**Proceedings of the Utah NASA Space Grant Consortium &
Annual Fellowship Symposium
UNSGC 2020
May 4, 2020, Provo, USA**

DJB2020

EFFECT OF SUPERHYDROPHOBIC SURFACE MICROSTRUCTURE ON TRANSIENT JET IMPINGEMENT COOLING

D. Jacob Butterfield*, John Morris, Julie Crockett
Fluids and Thermal Transport Laboratory
Department of Mechanical Engineering
Brigham Young University
Provo, Utah 84602

ABSTRACT

Jet impingement is an effective method of rapid surface cooling, and is highly dependent on surface condition and properties. Here, silicon surfaces are modified by ion-etching different micropatterns (posts or holes) on one side and coated with Teflon to make them superhydrophobic (SH). The other side of the surface has a screen-printed resistance heater. Surfaces are heated to temperatures between 200 to 320 °C, and then impinged on by a pure water jet at room temperature with flow rates ranging from 6 to 18 mL/s. Results show that there is little effect of microstructure, although hole surfaces and shorter microstructures tend to have slightly higher heat transfer. Heat transfer from the surfaces to the jet is shown to be highly dependent on jet flow rate, but not surface temperature.

NOMENCLATURE

a	jet radius
c_p	specific heat
k	thermal conductivity
Q	volume flow rate
q"	heat flux
r	radial distance from stagnation point
Re	jet Reynolds number
t	time
T_j	jet temperature
T_s	local surface temperature
v	velocity
W	Watts

Greek Symbols

δ	wafer thickness
ρ	density

Subscripts

si	Silicon
w	Water
H	Heater

INTRODUCTION

Jet impingement is known to be an effective method of rapidly cooling objects, even to small children blowing on food that is too hot. A constant lower-temperature fluid flow is introduced to the surface at an appreciable rate, which increases heat transfer. The properties of the jet fluid greatly impact the ability to remove heat; water conducts better than air and thus is used or considered in common applications such as metal quenching or nuclear-reactor emergency cooling [1, 2]. Other applications especially relevant to NASA where high amounts of thermal energy need to be removed efficiently include the high-power computing resources employed as well as rapid rocket launchpad cooling. Besides the jet itself, the material being cooled also plays a

*Address all correspondence to this author at jacob.butterfield@byu.edu.

significant role in heat transfer in this type of scenario [3], which is what is further explored in this work.

Initially, increasing surface temperature increases heat flux to a water jet as some of the energy transfer is in a latent form (boiling the water) creating a mixture of liquid and vapor flow. However, at a certain point the water cannot contact a surface due to all energy being transferred in a latent form and the flow becomes completely vapor. This is known as the Leidenfrost point, and actually transfers very little heat as water vapor has similar properties to an air jet. In this work, various superhydrophobic (SH) surfaces were superheated and impinged by water jets. Surface hydrophobicity affects the Leidenfrost point and thus the amount of heat that can be transferred from a surface.

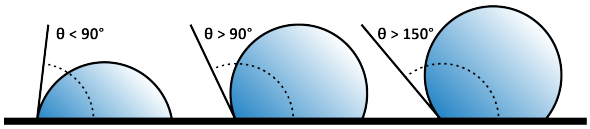

FIGURE 1: Contact angle is affected by the level of surface hydrophobicity, where hydrophobic surfaces have contact angles greater than 90° and SH surfaces have contact angles greater than 150°.

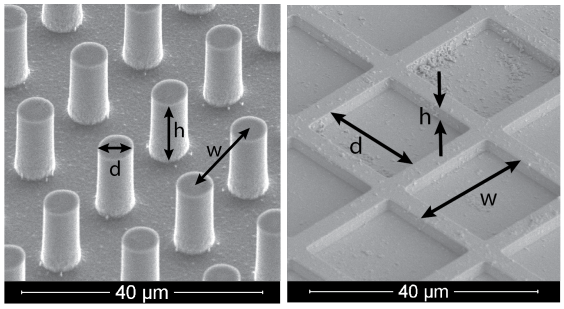

(a) **(b)**

FIGURE 2: (a) SEM image of round, post microstructures, with diameter (d), height (h), and pitch (w) labeled. (b) SEM image of square, hole microstructures with similar dimensional labeling.

Hydrophobicity is a measure of water's attraction to a surface relative to its cohesion to other water molecules. Hydrophobicity depends on surface chemistry, specifically on the material's surface energy. This changes the contact angle that a water droplet makes on a surface (see Figure 1). A hydrophobic surface can be made SH, or have a contact angle greater than about 150° by changing the geometry to include micro- or nano-scale roughness such as the micro posts and micro holes in Figure 2. The gaps in the microstructure provides a slip condition for water above it, reducing viscous shear in fluid flows. However, this reduction in contact also inhibits the ability for heat to be transferred from the surface. Furthermore, Leidenfrost effects can be enhanced on the surfaces because of the low contact and potential for vapor to flow through the microstructure, underneath a liquid layer.

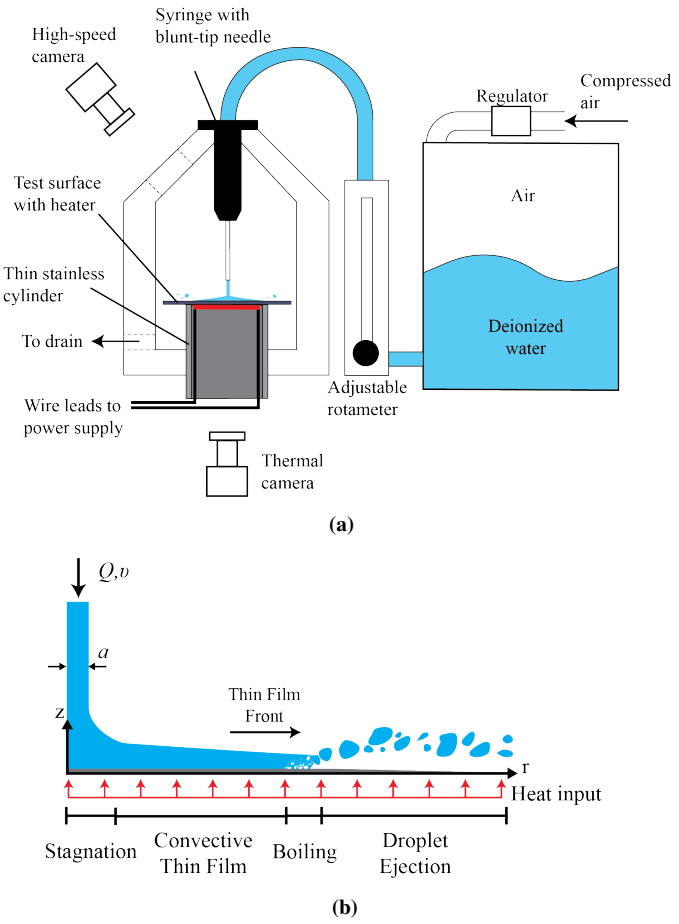

FIGURE 3: (a) Schematic of experimental apparatus and (b) enlarged radial cross-section of the jet and the regions of heat transfer across the surface.

In previous work, we have shown that SH surfaces have significantly slower cooling times due to lower heat fluxes compared to hydrophilic surfaces. Here, we further that work by examining the differences caused by varying surface geometry by modifying pitch, or the distance between features, feature height, and feature type (holes vs posts). These early results show that there is actually very little difference when varying each of these surface parameters, although the variability itself in the results is

TABLE 1: Surface fabrication parameters, as denoted in Figure 2.

Case Number	1	2	3	4	5	6	7	8
Holes/Posts (H/P)	H	H	P	P	P	P	P	P
Round/Square (R/S)	R	S	R	S	R	R	R	R
Height (μm)	15	15	15	15	25	15	5	15
Pitch (μm)	24	24	24	40	16	8	8	16
Width/Diam. (μm)	19	20.6	19	20	7	3.5	3.5	3.5
Cavity Fraction (%)	50	75	50	75	85	85	85	96

also high and thus further analysis is necessary. There may be an effect of decreased cavity fraction (ratio of etched area to total projected area) and shorter structures that increases liquid water contact with the surface, which in turn increases heat transfer to the jet. As seen in previous works, heat transfer is a strong function of jet flow rate, but as will be shown there are conflicting effects due to altering initial surface temperature that negate any trends based on modifying that parameter.

METHODS

Experimental Apparatus

To quantitate the heat transfer from superhydrophobic surfaces to an impinging jet, 525 μm thick silicon wafers with a diameter of 100 mm were used, with the superhydrophobic surface on the top opposite a wire resistance heater on the bottom. The wafers were first patterned using standard photolithography methods, then etched by a reactive ion etching (RIE) process to create the necessary microstructure. Several versions of superhydrophobic surfaces were fabricated as summarized in Table 1, with references to surface parameters shown in Figure 2. The surfaces then have a thin layer (100 nm) of chromium deposited via electron-beam evaporation followed by spin-coating a thin layer (200 nm) of natively hydrophobic DuPont™ Teflon® (commercial brand of polytetrafluoroethylene, PTFE).

The heaters have a diameter of 51 mm and overall resistance of 0.25 Ω and are fabricated by screen printing with a silver paste (ESL 599-E). The heater buses are connected via wire leads epoxied in place (Atom Adhesives AA-DUCT 2979) to a 20-V, 120-A DC power supply (HP 6011A). After screen printing, the heaters and back sides of the wafers are spray-painted with a flat black coating of known emissivity (ε = 0.97) to aid thermal imaging (Rustoleum® 248903).

During testing, the wafers are supported by a custom mounting apparatus (see Figure 3). The wafers, oriented with the superhydrophobic surface facing up, are placed upon a stainless steel, cylindrical tube with thin walls and relatively large thermal mass that inhibit significant conduction. A FLIR Thermal Imaging Camera is mounted beneath the hollow region of the cylinder to allow visual access to the bottom of the wafer mounted above it; thermal images are recorded at a rate of 200 Hz and a resolution of 320 by 256 pixels. High-speed images of the experiments are obtained by a Photron Fastcam APX RS located angularly above the wafer, which records images at a rate of 500 Hz and a spatial resolution of 1024 by 1024 pixels.

Water is supplied to the superhydrophobic surface through a long (15 cm) stainless steel nozzle of inner radius r_j = 1.275 mm situated 5 cm above the wafer, connected to a pressurized tank. The tank pressure determines the maximum jet flow rate while the flow is regulated and measured with a manual rotameter.

Experimental Procedure

Before conducting the experiments, each surface must be calibrated spatially and thermally to provide accurate comparison between the high-speed and thermal imaging. Once calibrated, power is increased until the wafer's resistance heater is raised to the experimental temperature as measured by the FLIR camera. The surface is considered sufficiently heated if both the temperature at the center of the wafer reaches the experimental temperature and there are no significant thermal disparities.

Once the surface is sufficiently heated, pure water is continuously impinged on its surface while recorded by the time-synchronized high-speed and FLIR cameras. Recording continues until the impinging water has reached steady state, defined to be a hydraulic jump of constant diameter and height with no apparent ongoing phase changes. The power connected to the resistance heater is then disconnected and the wafer is allowed to cool before conducting the next experiment.

Experiments are conducted while varying one of three parameters: (a) surface temperature (200, 280, or 320 ºC); (b) flow rate of impinging fluid (6, 12, or 18 mL/s); (c) surface type (round or square microposts or microholes). All experiments

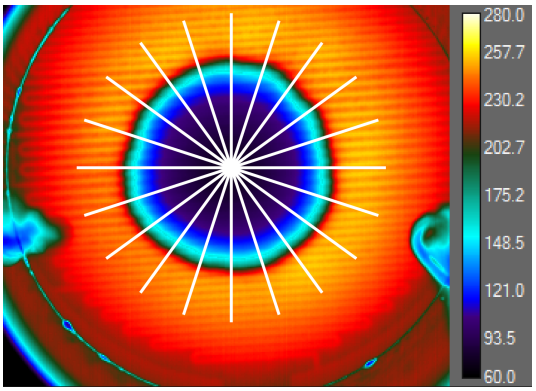

FIGURE 4: Thermal camera image of temperature (in °C) across the back side of a wafer. The alternating red and yellow lines are from the resistance heater, and the darker area shows the progression of the jet across the surface. White data-averaging radial lines are also shown.

varying surface temperature are conducted with a constant flow rate of 12 mL/s, while all experiments varying flow rate have a constant initial surface temperature of 280 ºC. Each experiment is conducted with each wafer a minimum of five times to account for statistical deviations, resulting in a total of 25 experiments per wafer. Observations of the surfaces during testing suggest no significant change in the hydrophobicity of the surface over the course of testing.

Analysis

The results from each experiment are processed using a MATLAB script to obtain the heat flux from the silicon wafer to the jet as a function of radius and time. This processing includes taking each image file and generating 20 evenly-spaced radial lines from the center of impingement, which are averaged to determine a radial temperature profile (see Figure 4). The temporal changes in temperature are also used to calculate local heat flux from the wafer to the water using the following equation:

$$q"(r,t) = \frac{\delta}{r}\frac{\partial}{\partial r}\left(k_{si} r \frac{\partial T}{\partial r}\right) + \frac{q_H}{\pi r_H^2} - \delta \rho c_p \frac{\partial T}{\partial t} \qquad (1)$$

where δ is the wafer thickness; r is the radial location; k_{si}, ρ, and c_p are the silicon thermal conductivity, density, and specific heat respectively as functions of the local wafer temperature, T; q_H and r_H are the heater power and heater area respectively; t is time relative to initial jet contact on the surface. This local heat flux was averaged over the area of the wafer to develop an average heat rate, and then integrated again over time to show how much total energy was transferred to the water as a function of time.

RESULTS

While the work is ongoing, several experimental test cases have already been performed, analyzed, and compared. First, a

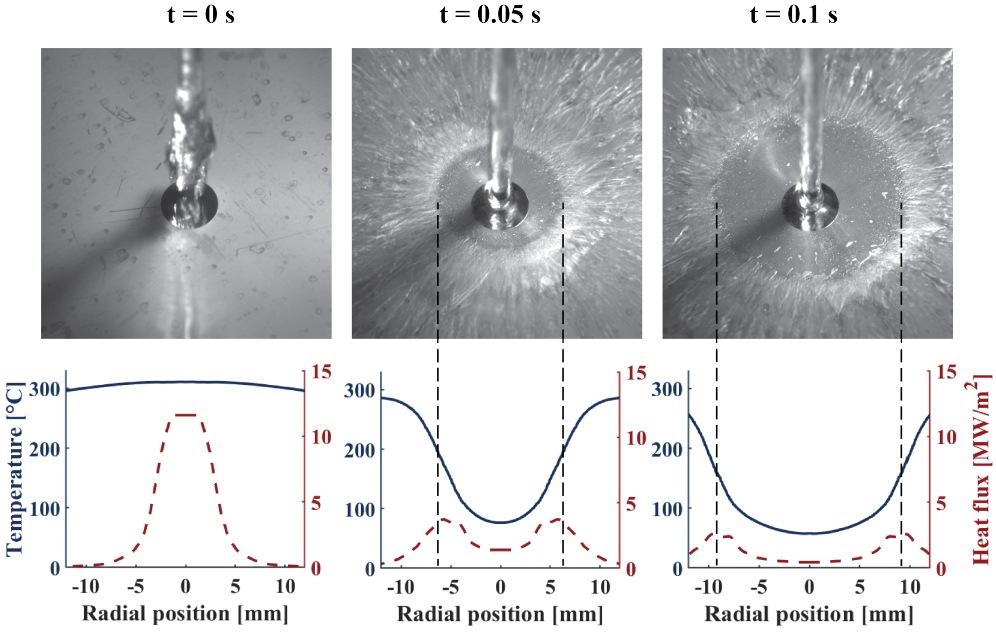

FIGURE 5: Impingement cooling progression for multiple times on a Case 4 surface with $T_0 = 320$ °C and Re_D = 12,000. Temperature and heat flux as functions of time and radial position are also shown.

comparison of the spreading rate, or how the thermal effects alter the hydrodynamics, will be discussed. Then, comparisons of heat transfer between surfaces will be shown.

Figure 5 shows results from the high speed camera and gives a reference for how the data is recorded and analyzed. High-speed images for a case 4 surface at $T_0 = 320$ °C and flow rate of 12 mL/s is shown for different times in the progression of impingement. The first image is just before impingement, while the subsequent times show how the thin film spreads across the surface. Spatially correlated temperature data from the thermal camera is shown below these images, along with the calculated local heat flux. It can be seen that the outside edge of where the liquid water contacts the surface corresponds quite well to the place of maximum heat flux for later times. This point is used to track how quickly the thin film contacts the surface.

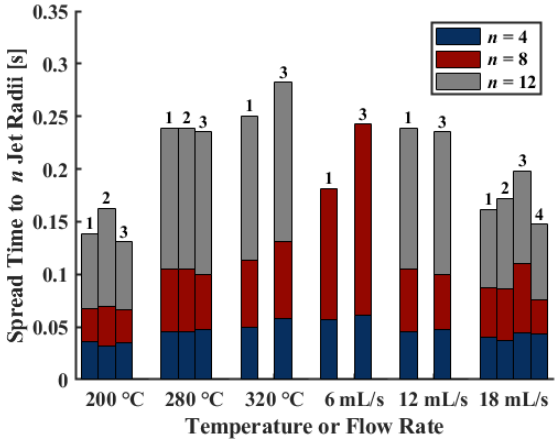

FIGURE 6: Thin film radius as a function of time for all hole surfaces and posts of corresponding cavity fraction for all temperatures and flow rates inspected.

The spreading rates for cases 1-4 are shown in Figure 6, which shows the time it takes for the thin film radius (defined by the vertical dashed lines in Figure 5) to reach different numbers of jet radii ($n = 4, 8, 12$) downstream of the stagnation point for the hole and post surfaces of equal cavity fraction. These times are shown plotted against the varying initial temperatures and flow rates for comparison. Shorter bars indicate faster times for the thin film to spread across the surface. In the case of the lowest flow rate (Re_D = 6,000), the thin film radius never reaches 12 jet radii downstream, as the hydraulic breakup radius is a function of flow rate. Data for all cases has not yet been acquired and analyzed, which is shown by the gaps in the data (such as cases 2 and 4 not appearing in the $T_0 = 230$ °C and 6 and 12 mL/s instances).

Comparing case 1 to 2 and case 3 to 4 both show how cavity fraction affects both holes and posts respectively at lower values. Comparing case 1 to 3 and case 2 to 4 shows same cavity fraction, but opposite microfeature type. General trends for these surfaces show that there is not a dependence on cavity fraction or microstructure geometry for these specific cases and conditions, as the values for all cases are similar for the same condition (within error).

There is a slight dependence of thin film spreading on initial surface temperature. As the surface gets hotter, it takes more time for the surface to cool to near saturation temperature via latent heat transfer (boiling), so that the water can then contact the surface and convectively cool it. There is a strong dependence on flow rate as well. The more momentum there is in the initial flow, the faster the thin film is able to spread along the surface. This can be as high as 50% longer to spread to $n = 12$ jet radii for case 1 when the flow rate is reduced from 18 to 12 mL/s.

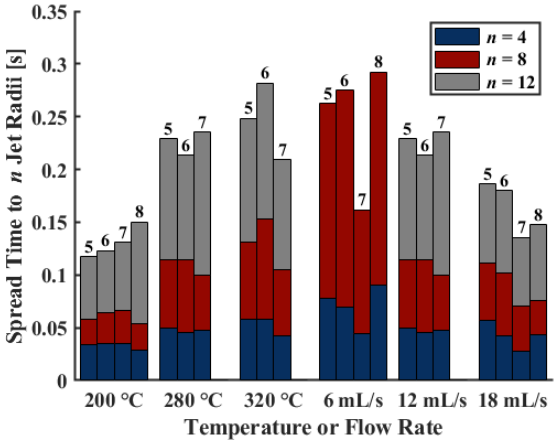

FIGURE 7: Thin film radius as a function of time for all post surfaces for all temperatures and flow rates investigated so far. This shows comparisons between post diameter and pitch, cavity fraction, and height.

Similar thin film spreading for cases 5-8 is shown in Figure 7, which compares posts based on microstructure. Case 5 has the highest height and diameter, but is equal in cavity fraction to cases 6 and 7, which are identical except for case 7 having shorter posts. Case 8 has the highest cavity fraction, but equal diameter posts as cases 6 and 7.

Overall trends here are similar to the previous comparison between posts and holes. There seems to be some small dependence on initial surface temperature, as the thin film spreads more quickly on the lowest temperature surface. There is also some function of flow rate involved, however much of the apparently large difference with low flow rate is mainly due to such low momentum that the thin film is never able to reach the further

downstream radii. There is relatively little difference between spreading on each of the surfaces for most of the cases based on microstructure variation, at least for this initial data.

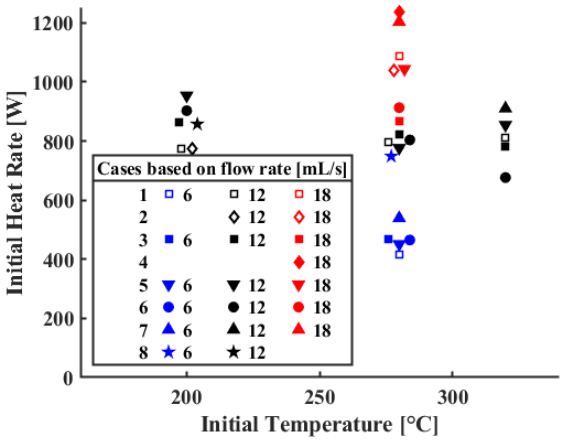

FIGURE 8: Initial average heat rate as a function of initial temperature and flow rate. Hollow and solid markers represent hole and post surfaces, respectively.

Heat transfer comparison is shown first by initial average heat rate over the camera viewing window. This calculated by integrating the local heat flux calculated with Equation 1 over this viewing window and dividing by that area. This value is relatively constant for the first 0.1 - 0.2 seconds of impingement, when most of the heat transfer from the surface occurs. The comparison is shown in Figure 8 for all cases and conditions tested so far. This initial average heat rate is plotted against the different temperatures, with colors denoting the different flow rates and different markers showing the different cases. All clusters of data were acquired at the standard surface temperatures, but are staggered in the plot for clarity.

Generally speaking, the difference between hole and post surfaces (open and solid markers) is minimal. The largest differences seem to be for low initial surface temperature or high flow rate, but the trend is not consistent.

As seen with spreading rate, there seems to be a large dependence on jet flow rate. As that parameter increases, heat rate tends to increase. Case 5, for example, increases in heat rate by 46% when the flow rate is increased from 6 to 18 mL/s. As this figure shows a comparison of energy transfer per unit time, it is logical that the rate at which water is able to contact the surface is directly correlated to the heat transfer rate.

There is not, however, a clear trend with initial surface temperature, as most data points for the 12 mL/s flow rate experiments all hover around 800 W regardless of temperature. This is a more complicated parameter than jet flow rate, because it affects both the total amount of energy available to be transferred (based on initial thermal storage in the wafer) as well as the liquid water's capacity to contact the surface (which is limited with increased temperature). This trade-off of increased initial energy and slowed thin film spreading reduces the impact of temperature on initial heat rate for the cases observed here.

Another general trend for the cases shown is that case 7, the case of the shortest posts, typically has a higher heat rate than most other surfaces, and it is always higher than case 6, which has identical geometry except for taller posts. With shorter posts, the possibility of penetrating the gaps and wetting within the microstructure is increased, which could lead to the apparent increase in heat transfer.

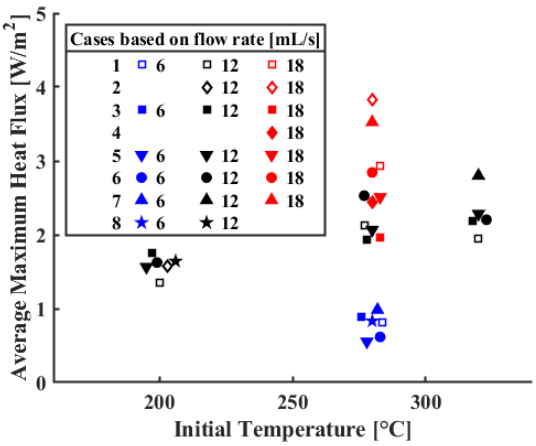

FIGURE 9: Averaged maximum heat flux compared for all surfaces as a function of flow rate and initial temperature.

Another method of comparing heat transfer is by using heat flux, or the heat rate per unit area. In this case, the maximum local heat flux past about 6 mm from the stagnation point slightly decreases linearly with radial position. In a similar way to the average heat rate, the maximum heat flux in this outer region was averaged and the results are compared in Figure 9 against temperature, which markers indicated cases and colors showing differences due to flow rate variation.

From this plot it can be seen that there is some dependence on flow rate, although that dependency is not quite as well-defined here, and in come cases such as case 3 there is hardly and difference between an increase in flow rate from 12 to 18 mL/s. However, for case 7 this heat flux value increases 123% when flow rate increases from 6 to 18 mL/s. On this heat transfer rate per unit area basis, there seems to be more of a trend of increased heat flux with increasing temperature, but it's only slight.

As with initial heat rate, there seems to be no clear distinction between hole and post surfaces generalized for all experimental conditions. However, for the highest flow rate it would appear that hole surfaces (cases 1 and 2, denoted by hollow markers) have significantly higher local heat fluxes compared to their post counterparts (cases 3 and 4, shown with the same shapes but filled). For that same experimental condition, these lower-cavity fraction cases (50 and 75%) trend to higher heat fluxes with lower cavity fractions. Case 7 surfaces (shortest posts) again seems to trend higher than other surfaces in regards to heat flux. This is again, potentially due to increased capacity for microstructure wetting, which increases liquid contact area with the surface, which would lead to increased heat transfer. Similarly, lower cavity fraction leads to increased surface contact and would imply higher heat flux. Further investigation is necessary to draw more concrete conclusions.

DISCUSSION

In this work, SH surfaces made of post or hole microstructures with varying height, pitch, and cavity fraction were used in a jet impingement heat transfer study. The water jet, at room temperature, varied in flow rate from 6 - 12 mL/s, and the initial surface temperatures varied from 200 - 320 °C. Surfaces were compared against each other to find which allowed for fastest liquid spreading across the surface, which increases heat transfer by allowing more rapid convection as well as latent heat loss in the form of boiling. For the surfaces examined here, holes and posts of equal cavity fraction did not seem to have an effect on thin film spreading for low cavity fractions (50 - 75 %). Comparing results for varying post structures showed similar results, with little noticeable difference based on altering post diameter, width, height, and cavity fraction.

Another method of comparing heat transfer was to look at the initial average heat transfer rate from the surface to the water, which showed the strongest dependency on flow rate and very little differences for surface type. A potential exception could be the case of shortest posts, which tended to have higher heat flux compared to surfaces that differed only by taller posts. Maximum heat transfer around the outer regions of the surfaces also allowed a method of comparison, and showed potential trends of decreased cavity fraction and feature height leading to higher averaged maximum heat flux.

Future work involves collecting data for all surfaces under all conditions to allow for more comprehensive comparison. Alternate methods of comparing data sets will be considered in order to better quantify any differences not discovered by the methods employed here. With all surface parameters explored, applications requiring the use of superheated SH surfaces in jet impingement cooling scenarios will be better equipped with the knowledge of how best to pattern surfaces to allow for maximum heat transfer.

REFERENCES

[1] Filipovic, J., Incropera, F. P., and Viskanta, R., 1995. "Quenching Phenomena Associated with a Water Wall Jet: II. Comparison of Experimental and Theoretical Results for the Film Boiling Region". *Experimental Heat Transfer,* ***8***(2), pp. 119–130.

[2] Mitsutake, Y., and Monde, M., 2001. "Heat transfer during transient cooling of high temperature surface with an impinging jet". *Heat and Mass Transfer/Waerme- und Stoffuebertragung,* ***37***(4-5), pp. 321–328.

[3] Mozumder, A. K., Monde, M., Woodfield, P. L., and Islam, M. A., 2006. "Maximum heat flux in relation to quenching of a high temperature surface with liquid jet impingement". *International Journal of Heat and Mass Transfer,* ***49***(17-18), pp. 2877–2888.